

# Investigation of Interstellar Object Flux Through the Solar System

by

Katherine M. Hahn

Submitted to the Department of Earth, Atmospheric, and Planetary  
Sciences

in partial fulfillment of the requirements for the degree of

Bachelor of Science in Earth, Atmospheric, and Planetary Sciences

at the

MASSACHUSETTS INSTITUTE OF TECHNOLOGY

May 2021

© Massachusetts Institute of Technology 2021. All rights reserved.

Author .....  
Department of Earth, Atmospheric, and Planetary Sciences  
May 14, 2021

Certified by .....  
Dr. Benjamin P. Weiss  
Professor of Planetary Sciences, Chair of the Program in Planetary  
Sciences  
Thesis Supervisor

Accepted by .....  
Dr. Richard P. Binzel  
Chair, Committee on Undergraduate Program



# Investigation of Interstellar Object Flux Through the Solar System

by

Katherine M. Hahn

Submitted to the Department of Earth, Atmospheric, and Planetary Sciences  
on May 14, 2021, in partial fulfillment of the  
requirements for the degree of  
Bachelor of Science in Earth, Atmospheric, and Planetary Sciences

## Abstract

Currently, the number of interstellar objects through the solar system is a key factor in creating engineering projects that will allow for ISOs to be studied more closely, revealing important information about planetary formation and star system history. Thus, a current observational upper limit of the number density of ISOs through the Solar System was calculated. An updated number density was calculated by incorporating two known ISOs into Engelhardt's previous estimates which were created through simulation of synthetic ISO detection through the Pan-STARRS1 telescope (Engelhardt 2014). The updated number density was estimated as  $0.11 \text{ AU}^{-3}$  and  $3 * 10^{-3} \text{ AU}^{-3}$  for an inert and active population of ISOs, respectively. As more ISOs are detected, it is estimated the number density will continue to increase following a Poisson Distribution until 15 ISOs have been detected at which point a new distribution should be invoked. The increased number density provides motivation for new scientific missions which will aim to explore complex topics such as planetary formation.

Thesis Supervisor: Dr. Benjamin P. Weiss

Title: Professor of Planetary Sciences, Chair of the Program in Planetary Sciences



## Acknowledgments

Foremost, I would like to thank my advisor Dr. Benjamin P. Weiss and other members of this project: Dr. Richard Linares, Daniel Miller, and Fitzgerald Duvigneaud for their continual support and guidance through the past year.

Secondly, I would like to thank Dr. Robert Jedicke for his help and allowing me to build off of previous work done by Toni Engelhardt under him. I am very appreciative of the collaborative environment we were able to build, your willingness to answer questions and help, and the hard work that went into prior work that builds the foundation for this thesis.

I am very appreciative of my peers in both the Earth, Atmospheric, and Planetary Sciences department and the Chemical-Biological Engineering department at MIT. Without you, I would not have made it through all four years of my education, and it definitely would not have been as fun. I would also like to thank both departments for giving me the opportunity to explore my passions while providing me with a welcoming space to do so.

Finally, I would like to my family and friends for their continued support throughout my life. Thank you all for being my sounding board and for reassuring me throughout this entire process. Without you, this would have been impossible.



# Contents

<b>1</b>	<b>Introduction</b>	<b>13</b>
1.1	Introduction . . . . .	13
1.1.1	Previous ISO Sightings . . . . .	14
1.1.2	Engineering Challenges . . . . .	16
1.1.3	Importance of this work . . . . .	17
<b>2</b>	<b>Methods &amp; Results</b>	<b>19</b>
2.1	Prior Work . . . . .	19
2.1.1	Overall Process . . . . .	19
2.1.2	ISO Generation . . . . .	20
2.1.3	MOPS Simulation . . . . .	21
2.1.4	Observational Number Density Limit Calculations . . . . .	25
2.1.5	Results . . . . .	30
2.2	Expanded Work . . . . .	34
2.2.1	Unique Object Classification and Analysis . . . . .	34
2.2.2	Updated Probability Distribution . . . . .	36
2.3	Updated Number Density Results . . . . .	38
<b>3</b>	<b>Discussion &amp; Conclusion</b>	<b>41</b>
3.1	Discussion . . . . .	41
3.1.1	Number Density Comparisons . . . . .	41
3.1.2	Future Estimations with New Surveys . . . . .	42
3.2	Conclusion . . . . .	44



# List of Figures

1-1	Orbital Path Definitions and Their Eccentricities . . . . .	14
1-2	Depictions of 'Oumuamua and Borisov . . . . .	15
1-3	Proposed Engineering Projects for ISO Studies . . . . .	17
2-1	Pan-STARRS1 Filter Efficiencies . . . . .	23
2-2	Fraction of Synthetic ISOs per Filter . . . . .	24
2-3	Cumulative Number of Objects Estimates for All $\alpha$ - $H'$ Combinations for Both Inert and Active Populations . . . . .	31
2-4	ISO Number Density Estimates for All $\alpha$ - $H'$ Combinations for Both Inert and Active Populations . . . . .	32
2-5	Filtered Simulated ISOs Compared to Two Known ISOs . . . . .	35
2-6	Probability Distributions for Two Known ISOs . . . . .	37
2-7	Probability Distributions for Upper Limits of Known ISOs . . . . .	37
2-8	$\rho_{IS}^{CL}(\alpha, H')$ as a Function of Number of Known ISO Events . . . . .	40
3-1	Upcoming Large-Scale Optical Telescopes . . . . .	43



# List of Tables

2.1	Original Summary of Number of Detectable ISOs, 90% Confidence Limit Density, and Volume . . . . .	33
2.2	Z-Scores for Confirmed ISOs versus Simulated ISOs . . . . .	36
2.3	Original Summary of Number of Detectable ISOs, 90% Confidence Limit Density, and Volume . . . . .	39



# Chapter 1

## Introduction

### 1.1 Introduction

Interstellar objects (ISOs) are astronomical objects in interstellar space that are formed outside of the Solar System and are not gravitationally bound to a star. Interstellar space is defined by the heliopause where the Sun's magnetic field and solar wind stop affecting their surroundings (NASA 2019). These objects are defined as having a hyperbolic orbit, meaning the eccentricity of the orbit is greater than 1 (Figure 1-1; NASA 1958).

Based on existing observations, ISOs have been shown to be either comets or asteroids. The former is a celestial body made of frozen ice, rock, and dust that often travels in an eccentric, elongated orbit around a star. The latter is a small, rocky object that is often jagged and irregularly shaped. Asteroids also generally travel in an elliptical orbit around a star. Both of these objects are formed from the remnants of planetary system formation processes as their accretion originated from material that was not incorporated into planets (NASA 2019). As a result, ISOs provide key insights into studying planetary formation processes as they relate to the Solar System and other planetary systems.

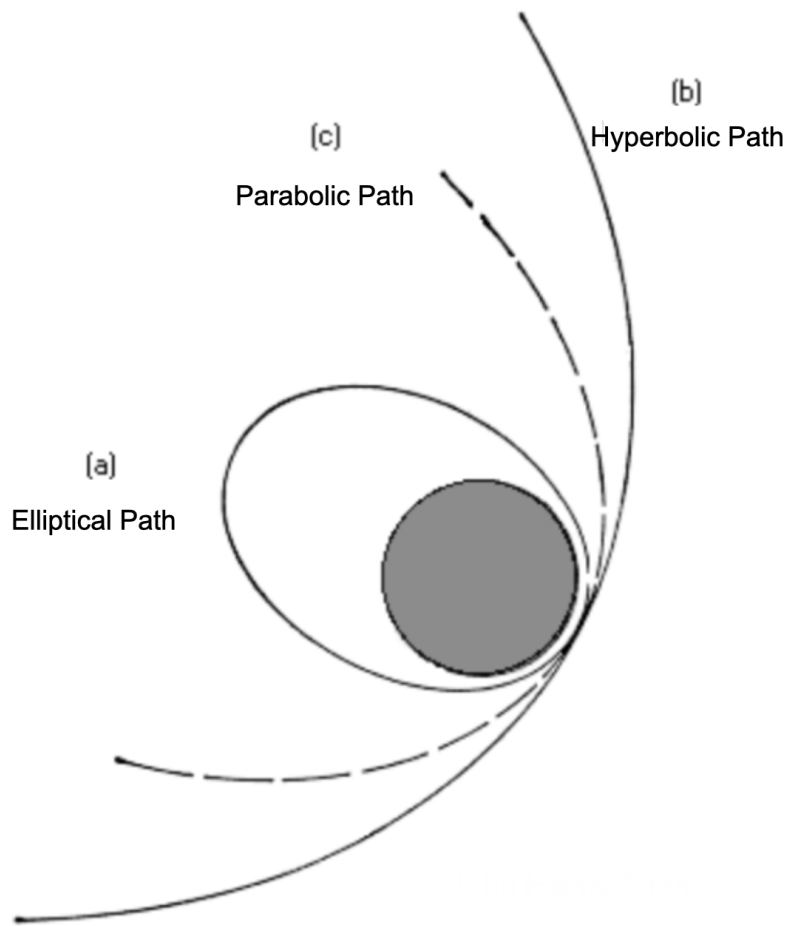


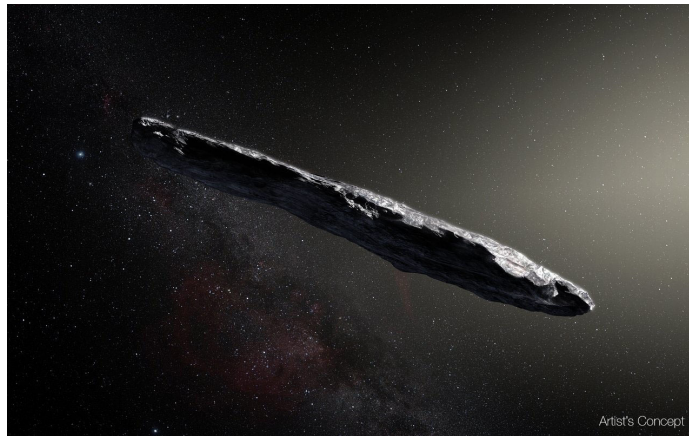
Figure 1-1: Various paths around a body of interest as noted by the dark circle. (a) The elliptical path represents a repeated trajectory with an eccentricity less than 1 of an object around the body of interest. (b) The hyperbolic path represents the path for objects with eccentricities greater than 1. ISOs follow hyperbolic paths through the Solar System. (c) The parabolic path represents the intermediate transition between the elliptical path and hyperbolic path (NASA 1958).

### 1.1.1 Previous ISO Sightings

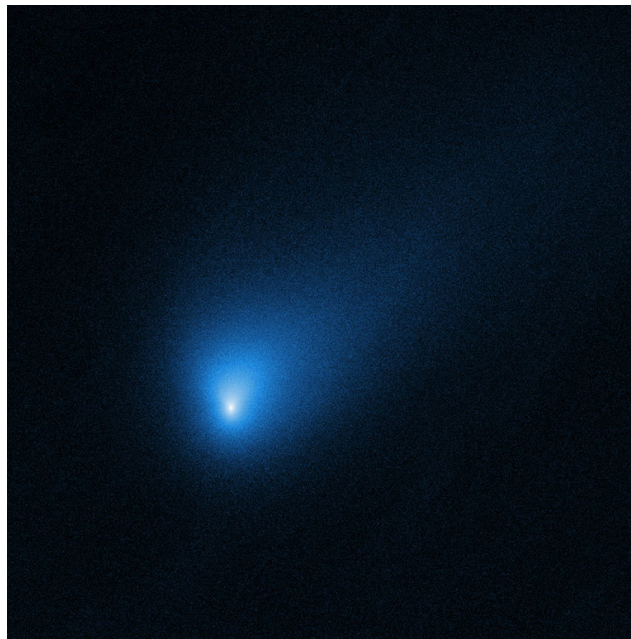
Currently, only two interstellar objects have been identified and widely confirmed by astronomers. The first, 1I/2017 U1 ('Oumuamua) was detected in 2017 by the Panoramic Survey Telescope and Rapid Response System (Pan-STARRS1 or PS1) telescope located at the University of Hawaii (Figure 1-2). 'Oumuamua was classified as an asteroid and had an estimated size of 35 by 200 kilometers in distance (Zuluaga 2018). The body was also estimated to have been traveling at a relative velocity of

$26 \frac{km}{s}$  with respect to the Sun (Zwart 2018).

The second object, C/2019 Q4 (Borisov), was discovered in 2019 by an astronomer in Ukraine (Figure 1-2). The comet was estimated to be approximately 0.975 kilometers across and 0.988 kilometers in length while traveling at a relative velocity of  $32 \frac{km}{s}$  with respect to the Sun (JPL 2019).



(a) 1I/2017 U1 ('Oumuamua))



(b) C/2019 Q4 (Borisov)

Figure 1-2: Two ISOs have been confirmed so far. (a) Artist depiction of 'Oumuamua (NASA Solar System 2019). (b) Hubble image of Borisov (NASA Solar System 2020).

As a result of the high relative velocities for each of these bodies, the Sun's gravity cannot deaccelerate the ISOs enough to trap them in the Solar System. Instead, the ISOs are ejected, limiting the time available for spacecraft to approach the object and gain important scientific measurements.

### 1.1.2 Engineering Challenges

As a result of the limiting hyperbolic excess velocity of ISOS, current propulsion technologies are a hindering factor in near-by ISO studies as detection infrastructure has a limited response time of a few months. This limited response time requires spacecraft to be prepared to approach the object at its high speed given the time window for observation is small.

There are currently new methodologies under development for the purpose of studying interstellar objects. One example of a methodology under development is a Dynamic Orbital Slingshot concept as suggested by Dr. Richard Linares of MIT. In this proposal, static satellites (statites) are enabled by solar sails that have a sufficient area to mass ratio to balance solar radiation pressure and the Sun's gravitational force. The statite is then able to hover indefinitely in the inner solar system and await the detection of a target ISO. In this state, the kinetic energy of the statite is zero, allowing for high potential energy. Upon receiving a detection signal, the statite re-orient its sail to slingshot into a freefall trajectory towards the Sun in a controlled manner as it makes use of its stored potential energy. Following this step, the statite enters directory into the rendezvous trajectory or completes a revolution around the Sun to align itself in the desired trajectory if needed. The statite is then able to complete rendezvous with an ISO where a successful rendezvous will lead to up close ISO studies using the statite's onboard sensors (Linares 2020; Figure 1-3).

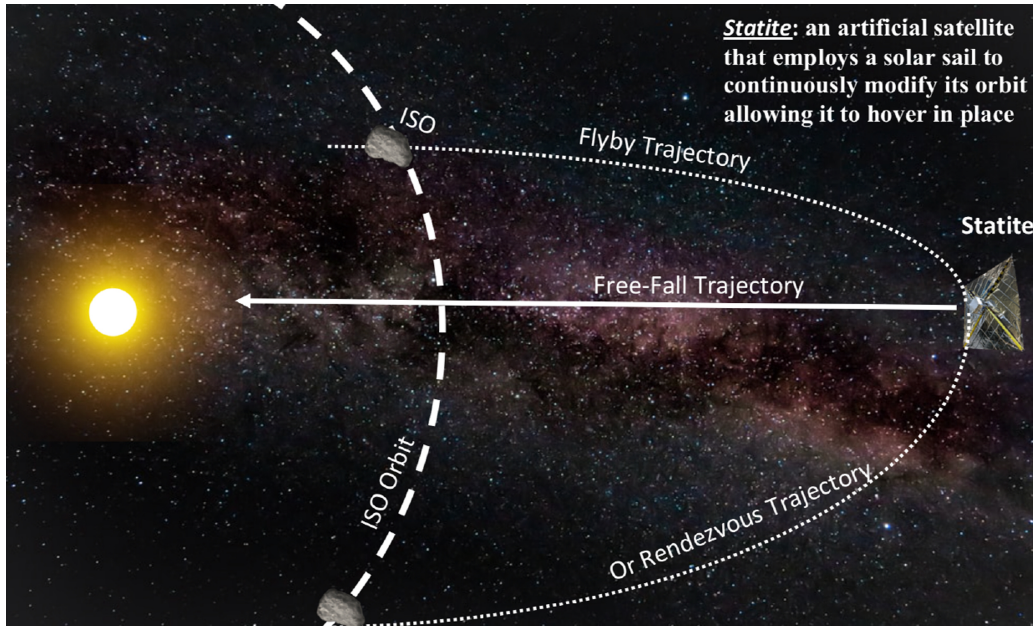


Figure 1-3: Static satellites (statite) represent an active project that could be used for rendezvous with ISOs to perform measurements with on-board sensors. The statite relies on its gravitational potential energy to be used as a slingshot into a freefall trajectory toward the path of the detected ISO (Linares 2020).

### 1.1.3 Importance of this work

For these scientific missions to be successful, it is important to understand the expected flux of ISOs into the Solar System as the flux will help determine where a statite can be placed in orbit and what technology can be used onboard for measurements. Previous studies have set out to classify the flux of ISOs through the solar system, but mixed results have been found.

In 2014, Toni Engelhardt of University of Hawai'i measured the observational upper limit of ISO spatial density with a 90% confidence limit to be  $5.4 * 10^{-2} \text{ AU}^{-3}$  in an inert, asteroid-like population and  $1.6 * 10^{-3} \text{ AU}^{-3}$  for an active, comet-like population for an  $\sim 1 \text{ km}$  diameter object. Comparably, Do et al. and Zwart et al. found values on the order of  $0.2 \text{ AU}^{-3}$  for 'Oumuamua sized objects (Do 2018; Zwart 2018). These value are similar to the value found by Engelhardt in 2017 as the object have sizes in different orders of magnitude. Additionally, McGlynn and Chapman as well as Jewitt calculated density values on the same order of magnitude at  $10^{-3} \text{ AU}^{-3}$

(McGlynn and Chapmann 1989; Jewitt 2003).

In contrast, these densities are at least one order of magnitude larger than others reported. Hughes et al. and Everhart et al. showed density values on the order of  $10^{-4}AU^{-3}$  (Hughes 2001; Everhart 1967). Futhermore, Stern et al. and Moro-Martín et al. found values on the order of  $10^{-6}AU^{-3}$  (Stern 1990; Moro-Martín 2009).

Despite the large range of differences in these values, only two papers accounted for 'Oumuamua-sized object observations, and none accounted for the discovery of Borisov. This work sets out to calculate an updated flux for ISOs through the solar system per cubic astronomical unit after accounting for the two known bodies using the Engelhardt 2014 thesis as a launching point. Through an updated probability assessment, a value of inert and active ISOs was calculated and compared to other estimates to determine a new observational upper limit on ISOs.

# Chapter 2

## Methods & Results

### 2.1 Prior Work

As previously stated, the prior work was performed by Toni Engelhardt of the University of Hawai'i at Mānoa's as a Master's thesis titled, "Setting an Observational Upper Limit to the Number Density of Interstellar Objects" in 2014 (Engelhardt ). This thesis was then supplemented by the Engelhardt et al. 2017 paper "An Observational Upper Limit on the Interstellar Number Density of Asteroids and Comets" as published in The Astronomical Journal (Engelhardt ).

#### 2.1.1 Overall Process

Engelhardt's master thesis quantified the observational upper limit of the number density of ISOs based on telescopic fields, efficiency, and simulated non-detections. This value was estimated through a 90% Poisson Confidence for asteroids and comets. These two bodies will be further referred to as inert objects, meaning no activity, and active objects, suggesting cometary activity. Engelhardt estimated these values through the following series of steps:

1. Given the thesis was written when no ISOs had been detected, ISOs were simulated using the Pan-STARRS1 (PS1) and Catalina Sky Survey as a basis for

the time period in which these ISOs were generated.

2. The efficiency of the PS1 telescope in each spectral filter was then determined and used to calculate the detection efficiency for each simulated object.
3. A size frequency distribution was applied to the objects which were then filtered for positive detection cases.
4. A Poisson confidence limit was used to determine the number density for both inert and active simulated bodies at a 90% confidence level.

These steps are described in more detail below as they pertain to validating and expanding Engelhardt’s estimations to include the two confirmed ISOs.

### 2.1.2 ISO Generation

For further detection efficiency simulations, a realistic ISO model was generated while accounting for gravitational focusing in a 2-body orbit propagation over the time interval  $T_p$ . Gravitational focusing refers to the increased probability that two objects will collide given their mutual gravitation attraction. First, the ISO model included gravitational focusing by distributing the ISOs homogeneously within a sphere of  $r_{init}$ . The relative velocity with respect to the Sun of the ISOs was then estimated to be in the same order as the velocity of surrounding stars. This distribution results in a Gaussian distribution with 99.7% of the simulated ISOs between  $v_{min} = 10 \frac{km}{s}$  and  $v_{max} = 40 \frac{km}{s}$  (Engelhardt 2014).

The propagation time was determined to be 71 years as it needs to account for the time that simulated ISOs that are randomly initialized in the Sun’s gravitational sphere need to leave the sphere to leave the model undisturbed. Additionally, the outflow of objects in the initialization sphere are not replaced, so the model density decreases over time. This new model density is considered a sphere with radius  $r_{valid}$ . The valid sphere radius ( $r_{valid}$ ) was set to 50 AU due to the limiting magnitude of

PS1. The initial radius and the valid sphere radius can be combined with margin factor ( $\eta$ ) to calculate  $T_p$  through

$$T_p = \eta \frac{2r_{valid}}{v_{min}}. \quad (2.1)$$

The time of initialisation was then calculated to be 27399 MJD using the fact that the model should be valid from January 1st, 2005 to January 1st, 2015 as these dates include PS1's and Catalina Sky Survey's duration. Next, 1.7 billion ISOs were generated before being filtered by eccentricity greater than 1 to find those on hyperbolic trajectories. The resulting 1 million ISOs were then propagated over 50,000 days using the OpenOrb n-body integrator incorporating the Sun, major planets, Pluto, and the Moon. Of these 1 million ISOs, approximately 35% were located within the valid modeling sphere and moved onto the next step (Engelhardt 2014).

Following initialization and propagation, the simulated ISOs orbital elements were used to calculate the model density over the valid sphere, resulting in an approximate model density  $\rho_{S,IS}$  of  $0.66 \text{ AU}^{-3}$ . First, the number of objects over heliocentric distances of 1 AU-50 AU. These values were then used to calculate the model density per cubic astronomical unit. The model density showed a peak at 0 AU due to the effect of gravitational focusing while 10 AU and further seems to have little effect from gravitational focusing. The model density  $0.66 \text{ AU}^{-3}$  at the furthest valid heliocentric distance (50 AU) was chosen to represent the model density at all points and defined at the model density in interstellar space  $\rho_{S,IS}$  (Engelhardt 2014).

### 2.1.3 MOPS Simulation

To determine which synthetic ISOs would be detected, the ISOs underwent a synthetic Moving Object Processing System (MOPS) simulation. Within PS1, the photometric system relies on five multi-spectral bands (cyan (g), red (r), yellow (i), blue (z), black (y)) and one wide-band comprised on three other bands (green (w) made up of g, r, and i). MOPS processing connects these bands to 2-4 detections of the same object

in a single night, referred to as tracklets. After obtaining these tracklets, a digest score is assigned by calculating the psuedo-probability between 0 and 100 where a higher digest score suggests a higher likelihood for the tracklet to belong to a certain sub-population. The digest score is calculated from each tracklet’s angular velocity, apparent magnitude, right ascension, and declination (Englehardt 2014).

After collecting the filter and digest score information, the detection, tracklet, and ISO efficiencies can be calculated using MOPS. Detection efficiency ( $\epsilon_d$ ) is defined as the probability that an object is registered as a detection by MOPS. This efficiency is mathematically defined as

$$\epsilon_d(V) = \frac{\epsilon_0}{1 + e^{\frac{V-L}{w}}} \quad (2.2)$$

where  $\epsilon_0$ ,  $L$ , and  $w$  are experimentally determined.  $\epsilon_0$  refers to the maximum efficiency that can be reached by bright objects on a specific night.  $V$  is the apparent magnitude, and  $w$  is the angular velocity.  $L$  is defined as the limiting magnitude and as the  $V$  value where  $\epsilon_d$  is 50% of  $\epsilon_0$ .

Tracklet efficiency  $\epsilon_t$  is defined as the number of objects in a field that create at least 1 tracklet with MOPS over the total number of objects in those fields. The relationship between detection and tracklet efficiencies was determined for the wide-band filter ( $w$ ) through experimental fitting exercises. The following set of equations was derived:

$$c_{\epsilon_0} = \frac{\bar{\epsilon}_{0,tf}}{\bar{\epsilon}_{0,df}} \quad (2.3)$$

$$c_L = \frac{\bar{L}_{0,tf}}{\bar{L}_{0,df}} \quad (2.4)$$

$$c_w = \frac{\bar{w}_{0,tf}}{\bar{w}_{0,df}} \quad (2.5)$$

where  $c$  represents the fitting factor for tracklet values denoted by the  $tf$  index which

refers to the tracklet value in a filter  $f$  and for detection values denoted by the  $df$  index in a filter  $f$ . Given these relationships, equation 2.2 can be rewritten for tracklet efficiency to

$$\bar{\epsilon}_t = \frac{\epsilon_{0,d} C_{\epsilon_0}}{1 + e^{\frac{V - L_d c_L}{w_d c_w}}} \quad (2.6)$$

where  $\bar{\epsilon}_t$  represents the tracklet efficiency (Engelhardt 2014).

The tracklet efficiencies for each filter can be plotted and compared using parameters provided (Figure 2-1). Comparison of each filter shows that all filters had an efficiency greater than 0.5, but the g filter was the strongest at 0.69 followed by the wide-band filter w at 0.6798 (Engelhardt 2014). The [r,r] filter was most common for all detected ISOs (digest score greater than 90) and showed a filter efficiency of 0.66, skewing the average efficiency of all detected bodies slightly below the highest efficiency filters (Figure 2-2).

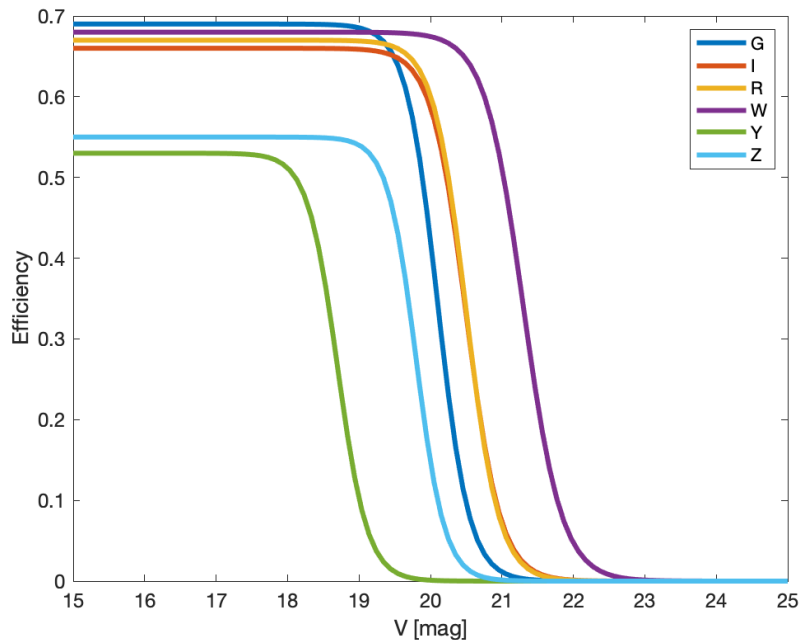


Figure 2-1: Six spectral-bands were used on PS1 and had different efficiencies. The most common filter was [r,r] which has an efficiency of 0.66, less than the 0.69 and 0.6798 from the g and w filters respectively.



The third efficiency that can be computed through the MOPS system is ISO efficiency. The ISO efficiency is defined as the combined efficiency with which an object can create a tracklet in the MOPS database and receive a high digest score, before being submitted for a follow-up and discovered as an ISO. This efficiency builds on the definition that the probability of an event happening at least once out of  $n$  times is

$$P_{combined} = 1 - \prod_n [1 - P_n] \quad (2.7)$$

where  $P_n$  is the probability that the event  $n$  has a positive outcome. This definition can be expanded to ISO efficiency as

$$\epsilon_{ISO,i} = 1 - \prod_{n_i=1}^{N_t} [1 - \bar{\epsilon}_{t,nf}(V_i)\mathcal{H}(D_{n_i} - 90)] \quad (2.8)$$

where  $i$  refers to a unique object ID,  $n_i$  refers to a unique tracklet ID of a tracklet ID that has object ID  $i$ ,  $\bar{\epsilon}_{t,nf}$  is the average tracklet efficiency in a certain filter  $f$  and  $\mathcal{H}(D_{n_i} - 90)$  represents the Heaviside function of the digest score  $D_n$  for each tracklet  $n$  (Engelhardt 2014). This efficiency is directly used in calculating the number of detected objects for the inert and active populations simulated.

## 2.1.4 Observational Number Density Limit Calculations

### Number Density Derivation

To calculate the observational upper limit of the ISOs, the steady-state number density should be calculated using the number of ISOs and the volume that they are located in. Initially, the steady-state number density of ISOs can be rewritten as

$$\rho = \frac{\tilde{N}}{V} \quad (2.9)$$

where  $\tilde{N}$  represents the average number of ISOs located within the volume  $V$ . This density relationship assumes an average number density that has a constant average

over a time interval much larger than the observation time interval. In this system, the volume estimate can refer to multiple types of volumes in the system. Firstly, the accessible volume of the system refers to the volume of space that falls within the radius determined by the limiting magnitude of the PS1 and subtracts the volume of space between the Earth and the Sun where no observations occur. Additionally, the Independent Effectively Observed Volume (IEOV), notated as  $\tilde{V}$ , refers to the equivalent volume that was observed with an efficiency of 1 with the PS1 MOPS system. The IEOV can then be subbed into equation 2.9, showing that the observational form of the steady-state number density can be written as

$$\rho = \frac{\tilde{N}}{\tilde{V}} \quad (2.10)$$

where  $\tilde{N}$  is determined with a statistical estimator and  $\tilde{V}$  is determined using MOPS (Engelhardt 2014).

To accurately determine the number of expected ISOs and the ISO number density at a 90% confidence level, a Poisson distribution should be used to determine the expected number of ISOs in the IEOV,  $\tilde{V}$ . The Poisson Distribution takes the form

$$P_{\lambda}(k) = \frac{\lambda^k e^{-\lambda}}{k!} \quad (2.11)$$

where  $P_{\lambda}(k)$  is the probability for a given number of events  $k$  that happen in a fixed interval of time or space where the average number of events is  $\lambda$ . The Poisson Distribution assumption holds if the average number of events is small in a large data set of repeated measurements collected under identical conditions. Here,  $k$  refers to the number of confirmed ISOs while  $\lambda$  refers to the expected number of ISOs. The Poisson distribution equation can be used to solve for the number of expected ISOs after providing the probability (0.1 for 90-percent confidence limit) and the number of confirmed ISOs (0 for initial estimates as no ISOs had been discovered). The expected number  $\lambda^{C.L.}$  can be subbed into the number density formula as  $\tilde{N}$ , resulting a new steady state density of

$$\rho^{C.L.} = \frac{\lambda^{C.L.}}{\tilde{V}} \quad (2.12)$$

where  $\rho^{C.L.}$  is the number density at the given confidence interval and  $\tilde{V}$  is the IEOV as before.

To obtain a final formula for the number density that can be modeled with the simulated ISO population,  $\tilde{V}$  can be rewritten through MOPS simulation relationships for the number of discoverable objects  $N_S(\alpha, H')$  and the number density distribution of ISOs in the simulation  $\rho_{S,IS}$ . Here, S is used to denote all variables from the origin of the PS1 survey and MOPS simulation. Within the MOPS simulation, the IEOV of a simulation volume  $\tilde{V}_S$  is identical to  $\tilde{V}(\alpha, H')$  if the parameters of the simulation are identical to those of the observational IEOV. The equation for the observations IEOV is as follows:

$$\tilde{V}(\alpha, H') = \int_{-\infty}^{H'} \int_{T_{survey}} \int_{V_A} \epsilon(\vec{r}, \vec{\xi}, \alpha, H', t) dV dt dH \quad (2.13)$$

where  $\alpha$  is the slope parameter of the size frequency distribution,  $H'$  is the absolute magnitude of the limiting ISOs at which the size frequency distribution is stopped,  $T_{survey}$  is the length of the PS1 survey,  $V_A$  is the volume of the valid sphere,  $\epsilon$  is the average ISO detection efficiency for objects position at  $\vec{r}$ ,  $\vec{r}$  is the position vector in a heliocentric frame, and  $\vec{\xi}$  is the set of orbit element distributions of ISOs.

Given that the parameters are identical,  $\tilde{V}_S(\alpha, H')$  can be set equal to  $\tilde{V}(\alpha, H')$  where  $\tilde{V}_S(\alpha, H')$  can be rewritten as

$$\tilde{V}_S(\alpha, H') = \frac{\tilde{N}_S(\alpha, H')}{\rho_S(\alpha, H')} \quad (2.14)$$

where  $\rho_S$  is the average density of  $\tilde{V}_S$ . As a result of the number density of ISOs in the model being much greater than the true number density,  $\tilde{N}_S(\alpha, H')$  can be rewritten as

$$\tilde{N}_S(\alpha, H') = N_S(\alpha, H') \quad (2.15)$$

where  $N_S(\alpha, H')$  is the number of objects that can be discovered. Furthermore, the average density should be converted to the previously measured  $\rho_{S,IS}(\alpha, H')$ . For fixed parameters in  $\tilde{V}$  and assuming that the orbit distribution is identical for real ISOs and the simulated ISOs, the average density can be related to  $\rho_{S,IS}(\alpha, H')$  through

$$\rho_S(\alpha, H') = \rho_{S,IS}(\alpha, H'). \quad (2.16)$$

Equations 2.15 and 2.16 can be substituted in 2.14 before being substituted into equation 2.12. These equations result in the number density limit of ISOs in interstellar space  $\rho_{IS}^{C.L.}(\alpha, H')$  in the form

$$\rho_{IS}^{C.L.}(\alpha, H') = \frac{\lambda^{C.L.}}{N_S(\alpha, H')} \rho_{S,IS}(\alpha, H'). \quad (2.17)$$

Here,  $N_S(\alpha, H')$  is determined by filter efficiency through

$$N_S(\alpha, H') = \sum_i [1 - \prod_{n_i=1}^{N_t} [1 - (\bar{\epsilon}_{t,nf}(V_i) \mathcal{H}(D_{n_i} - 90))] ] \quad (2.18)$$

where  $i$  refers to a unique object ID,  $n_i$  refers to the  $i^{th}$  unique tracklet ID,  $\bar{\epsilon}_{t,nf}$  is the average tracklet efficiency in a certain filter  $f$  and  $\mathcal{H}(D_{n_i} - 90)$  represents the Heaviside function of the digest score  $D_n$  for each tracklet  $n$  (Engelhardt 2014).

## Size Frequency Distribution

To determine  $\alpha$  and  $H'$  for the next steps of the number density calculation, the size frequency distribution was assigned using an exponential function of

$$\rho(H) = \rho_0 10^{\alpha(H-H_0)} \quad (2.19)$$

where  $H$  is the absolute brightness of the object,  $\rho_0$  is the density of ISOs with absolute

magnitude  $H_0$ , and  $\alpha$  is the slope parameter which determines the steepness of the function. For all  $\alpha$ - $H'$  combinations, a new corrected apparent magnitude  $V$  can be calculated using

$$V(H) = V_0 + H_{new} \quad (2.20)$$

where  $V_0$  is the original magnitude for each object as computed by MOPS where  $H=0$ , and  $H_{new}$  is a randomly assigned absolute magnitude as determined by

$$H_{random} = \log_{10}\left(\frac{X_u}{\alpha}\right) + H_0 \quad (2.21)$$

where  $X_u$  is a uniformly distributed random variable ranging from 0 to 1 (Engelhardt 2014).

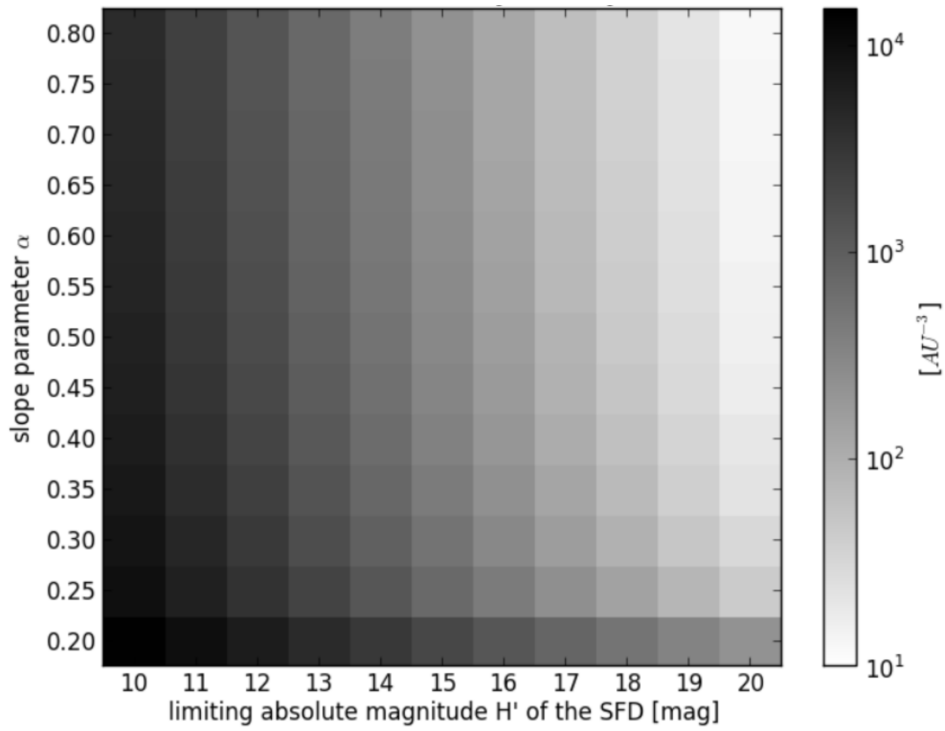
### Digest Score

The digest score for each object was automatically calculated in the MOPS simulation using a complex algorithm implemented in C that was not provided. The value is dependent on the apparent magnitude and recalculated for each new volume assigned to the object through the SFD distribution. As a result of the complexity of the calculation, a set of initial digest scores was calculated for each  $H'$  where  $H'$  ranged from 0 to 20 which were then used in the next steps as an approximation for the actual value.

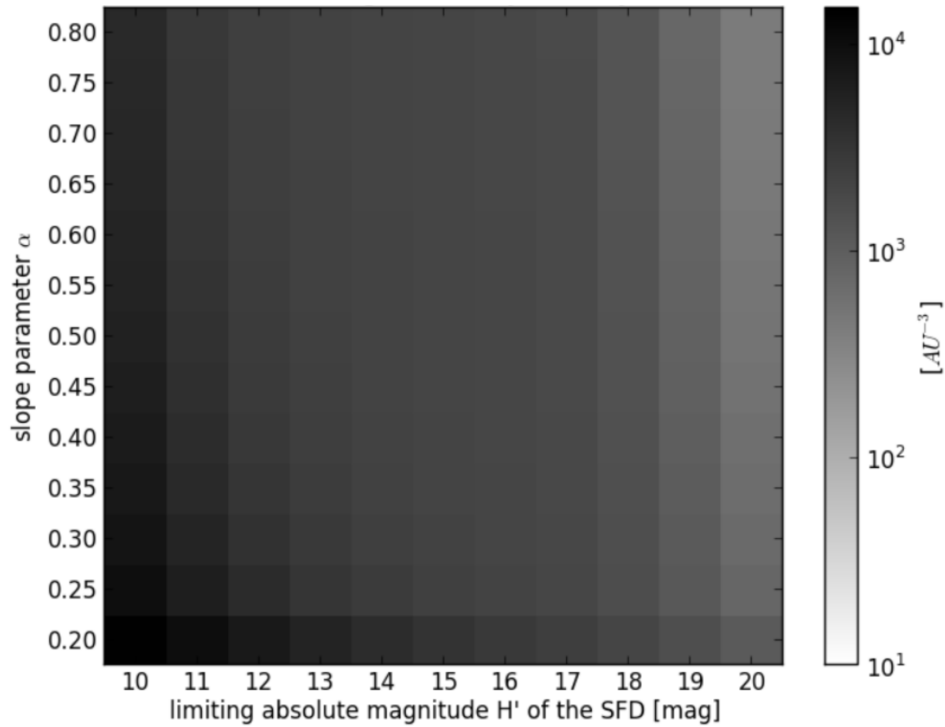
To compute the number density limit of ISOs, Engelhardt implemented a Python script to calculate  $N_S(\alpha, H')$  which could then be plugged into equation (2.10) with  $\lambda^{C.L.}$  and  $\rho_{S,IS}(\alpha, H')$ . The script looped through all  $\alpha$  and  $H'$  combinations and looped through every tracklet for each. For each tracklet, a random  $H$  value was assigned, resulting in a new correct apparent magnitude  $V$ .  $V$  was then used to determine the pre-computed digest score which was used to calculate the efficiency. Each tracklet was looped over 10 times while maintaining the same SFD but assigning a new  $H$  value. The numbers for all discovered objects were then averaged and used to calculate  $N_S(\alpha, H')$ . This process was repeated for both inert bodies on their own and for the combined population of both active and inert bodies (Engelhardt 2014).

### 2.1.5 Results

To estimate the number of ISOs  $\lambda^{C.L.}$  at a 90% confidence level, equation 2.11 was solved for  $\lambda^{C.L.}$  with a 10% probability and zero events as no ISOs had been confirmed at the time of publication. The equation resulted in  $\lambda^{C.L.} = 2.30$  which was then directly substituted into equation 2.17. The values of  $N_S(\alpha, H')$  were estimated and plotted over all  $\alpha - H'$  combinations for both inert and active bodies (Figure 2-3). These values were then substituted into (2.10) with  $\lambda^{C.L.} = 2.30$  and  $\rho_{S,IS}(\alpha, H') = 0.66 \text{ AU}^{-3}$  to calculate the observational number density limit for all  $\alpha - H'$  combinations (Figure 2-4).

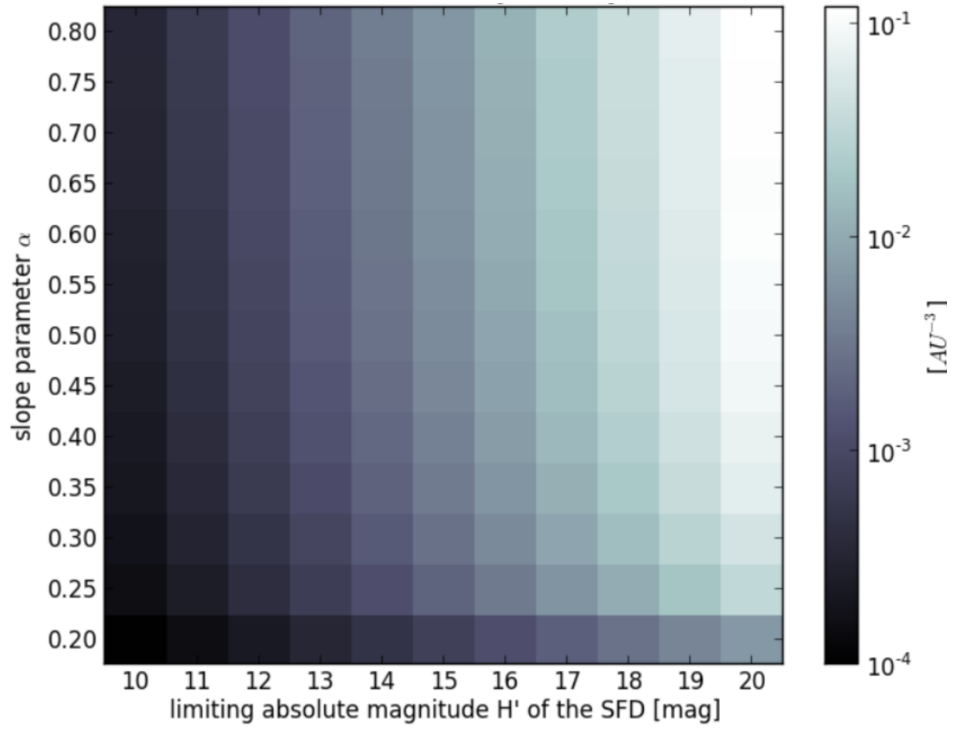


(a) Inert Population

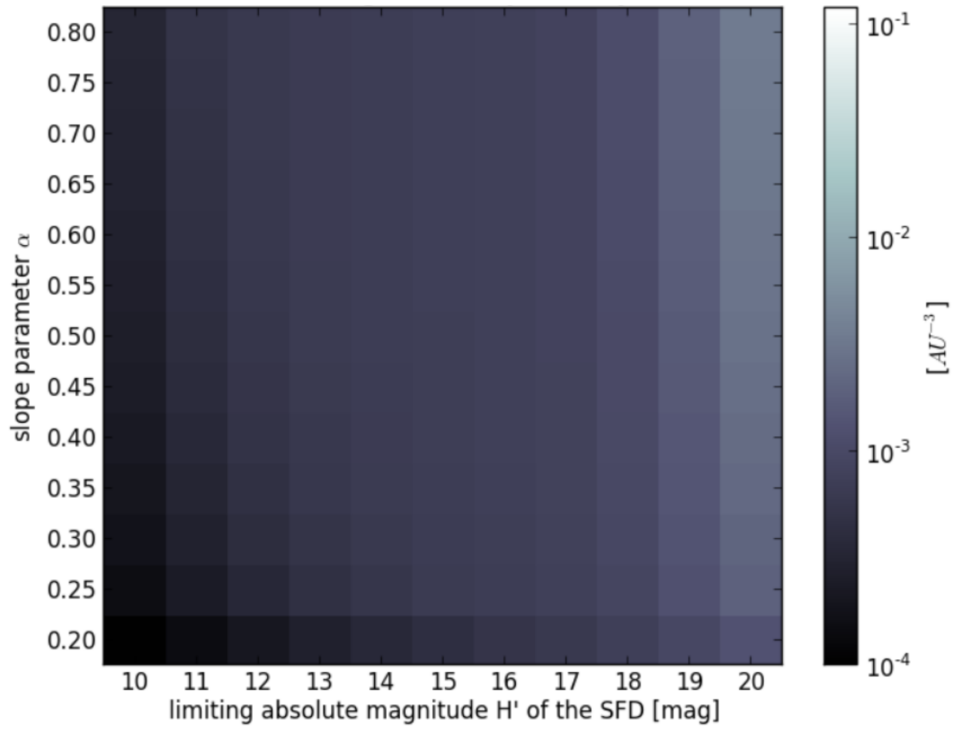


(b) Active Population

Figure 2-3: The cumulative number of objects for inert and active populations was calculated and plotted for all  $\alpha$ - $H'$  combinations (Engelhardt 2014).



(a) Inert Population



(b) Active Population

Figure 2-4: The cumulative number of objects was used to calculate the number density for inert and active populations which was then plotted for all  $\alpha$ - $H'$  combinations (Engelhardt 2014).

Through this analysis, the SFD parameters were set to be 0.5 and 19 for  $\alpha$  and  $H'$  as these values correspond to an  $\sim 1$  km diameter object. Thus, the observational limit was determined to be  $5.4 * 10^{-2} \text{ AU}^{-3}$  in an inert population and  $1.6 * 10^{-3} \text{ AU}^{-3}$  for an active population for an  $\sim 1$  km diameter object. Using equation 2.12, an IEOV of  $42.9 \text{ AU}^3$  and  $1,411 \text{ AU}^3$  for an inert and active population, respectively (Table 2.1; Engelhardt 2014).

Population	$N_S(\alpha, H')$	$\rho_{IS}^{C.L.}(\alpha, H') (\text{AU}^{-3})$	IEOV ( $\text{AU}^3$ )
Inert	28.11	$5.4 * 10^{-2}$	42.9
Active	948.75	$1.6 * 10^{-3}$	1,411

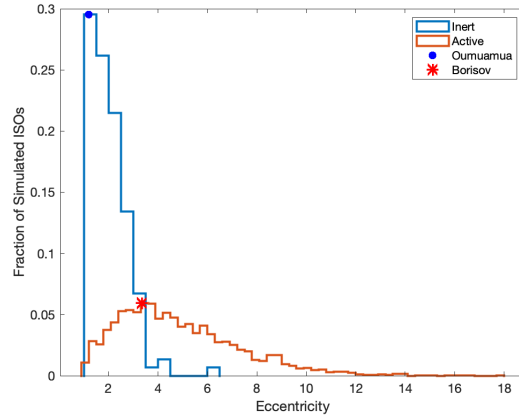
Table 2.1: Summary of Number of Expected ISOs, 90% Confidence Limit Density, and Volume for each population. The inert population had a lower number of detectable ISOs and IEOV but a higher number density compared to the active population (Engelhardt 2017).

## 2.2 Expanded Work

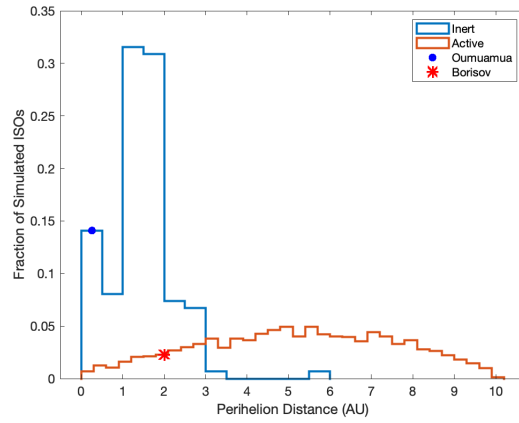
### 2.2.1 Unique Object Classification and Analysis

To begin updating the Engelhardt work to a more accurate value, a unique list of detected ISOs was gathered for further assessment. First, an undergraduate student working under Dr. Richard Linares, Fritzgerald Duvigneaud, collected the list of orbital elements, tracklet efficiencies, and digest scores for the simulated ISOs from the Engelhardt team. Duvigneaud filtered the ISOs to create two lists of unique objects: one list for inert objects and one list for active objects using the raw ISO simulation data. Following initial filtering, Duvigneaud created two additional lists of non-unique objects that had a digest score greater than 90 for both the inert and active populations that were provided by the Engelhardt team. A cutoff of 90 was chosen as 90 is the baseline digest score for an object to be classified as detected. Duvigneaud's four lists were then used as inputs for a python script to combine the lists into two inventories that could be used for furthering Engelhardt's initial work. Each list was comprised of unique simulated ISOs that had the required digest score for both inert and active populations. This python script relied on matching the tracklet ID and SSM ID for each unique object in its respective population list before the orbital elements and digest score were copied and assigned to the object in the final inventories.

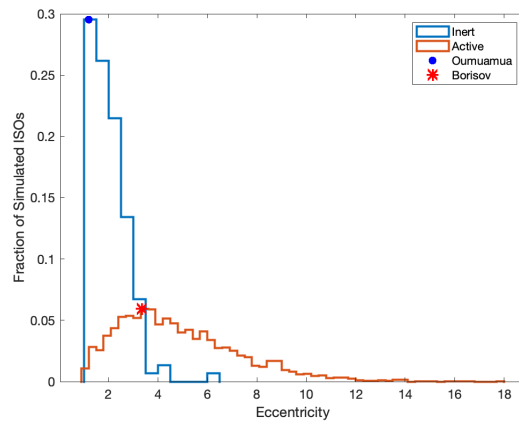
To better understand the simulated detected ISO population, various orbital elements were studied and plotted against the known values of the two confirmed ISOs ('Oumuamua and Borisov). The eccentricity, perihelion, and inclination were chosen as the primary orbital elements to be studied as these values were readily available for the simulated ISOs and in literature for 'Oumuamua and Borisov (Figure 2-5).



(a) Fraction of Objects versus Eccentricity



(b) Fraction of Objects versus Perihelion



(c) Fraction of Objects versus Inclination

Figure 2-5: The fraction of simulated ISOs were plotted against eccentricity, perihelion, and inclination to assess how the two known ISOs compare to the synthetic ISO sample. For each parameter, the value associated with each of the two known ISOs were plotted and fell within the synthetic ISO distribution.

For each orbital element plotted, the two known ISOs could be plotted on the histogram for the simulated ISOs. The plotted relationships for the known and simulated ISOs strengthen the feasibility of the simulated ISOs modeling realistic ISOs. The z-scores for the two known objects were calculated and compared to the simulated ISOs to better show how 'Oumuamua and Borisov compared to Engelhardt's simulated ISOs (Table 2.2). These values show that 'Oumuamua and Borisov are within two standard deviations of the inert and active populations respectively. Thus, the synthetic populations are valid models based on the known ISO values.

Object	Perihelion	Eccentricity	Inclination
'Oumuamua	-1.52	-1.12	0.38
Borisov	-1.37	-0.60	-1.74

Table 2.2: Z-Scores for 'Oumuamua and Borisov were calculated to compare the confirmed ISOs to the synthetic ISOs used for modeling. Each value fell within 2 standard deviations or less of the population mean, showing that the known ISOs fit well within the synthetic population.

### 2.2.2 Updated Probability Distribution

As done in the Engelhardt thesis, a Poisson distribution with a 90% confidence interval was used to calculate an updated value for the average number of events  $\lambda^{C.L.}$ . A methodology similar to that found in the original work was used; however, the given number of events  $k$  was updated to account for the discovery of 'Oumuamua and Borisov since Engelhardt published his work. The formula then led to multiple solutions rather than one solution as in the case for zero known events (i.e.  $k=0$ ) (Figure 2-6). For each solution, the number density was calculated, and the largest solution was chosen as it corresponded to the upper limit first described by Engelhardt (Figure 2-7).

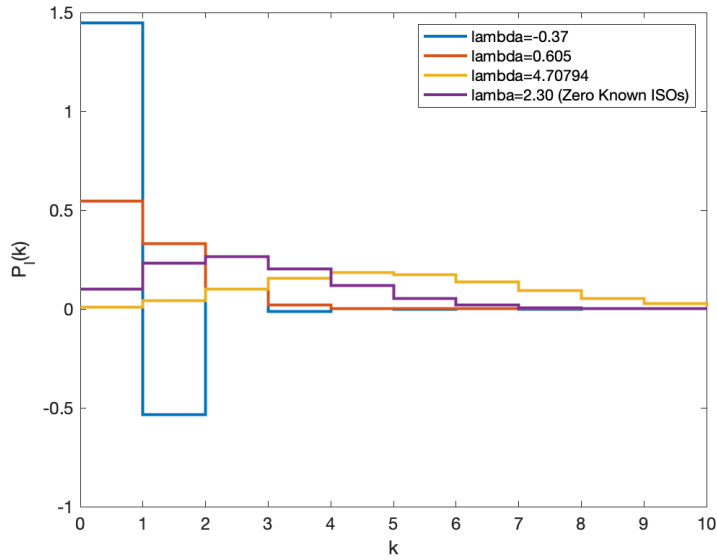


Figure 2-6: For two known ISOs, three solution exist for the Poisson Distribution. These can be compared to the original Poisson Distribution provided by Engelhardt at zero known ISOs.

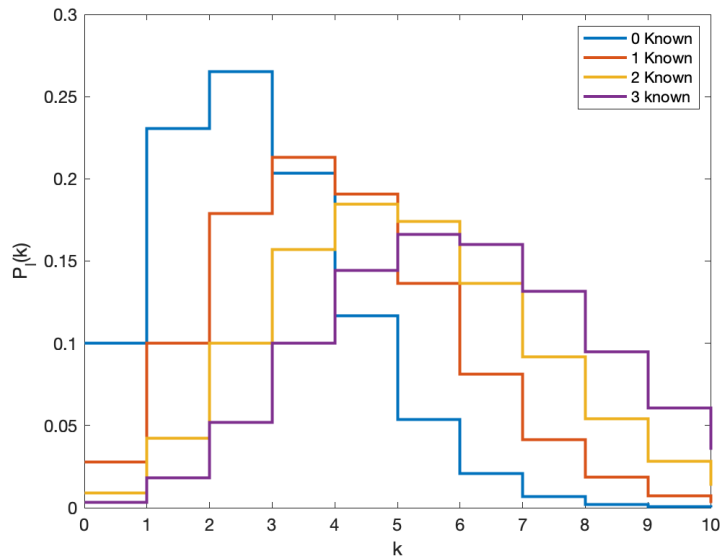


Figure 2-7: The highest  $\lambda$  solution was used to compute the upper limit of the number density. This  $\lambda$  solution was used to graph the Poisson distribution for 0-2 known ISOs which showed a shift toward the right with more confirmed events.

The same process was followed to determine how the average number of events and the number density would change with more ISO sightings. Whole number increments from  $k=0$  to  $k=20$  as  $k$  must physically be a whole number given that it represents the number of ISO sightings over time. Using this  $k$ -range, the Poisson distribution provided realistic numbers until  $k=16$  at which the results became negative and nonphysical (Figure 2-8). Results including and after  $k=16$  were disregarded in studying how the number density changes with each new sighting. The cause of this discrepancy at  $k=16$  is unknown but may be caused by a transition in the model that occurs when there are too many sightings for the Poisson distribution to remain accurate.

## 2.3 Updated Number Density Results

After calculating the average number of ISOs, the number density can be recalculated using the same  $N_S(\alpha, H')$  and  $\rho_{S,IS}(\alpha, H')$  as used by Engelhardt after providing an updated  $\lambda^{C.L.}$ . As a result of the digest code being unavailable, the  $N_S(\alpha, H')$  was back calculated for an inert and active population as determined by the original number density calculation. Solving equation 2.17 for  $\rho_{S,IS}(\alpha, H')$  and using the  $\rho_{IS}^{C.L.}(\alpha, H')$  values determined by Engelhardt,  $N_S(\alpha, H')$  is approximately 28.11 and 948.75 for inert and active populations respectively. Again,  $\rho_{S,IS}(\alpha, H')$  was assumed to be equivalent to  $0.66 \text{ AU}^{-3}$  for each  $\lambda^{C.L.}$  studied. For updated number density calculations,  $N_S$  and  $\rho_{S,IS}(\alpha, H')$  were held constant as the values were calculated from the simulated ISO population which has not changed.

Assuming 2 confirmed ISOs ('Oumuamua and Borisov), an updated upper limit number density of ISOs is shown to be  $0.11 \text{ AU}^{-3}$  and  $3 * 10^{-3} \text{ AU}^{-3}$  for inert and active populations respectively. These values correspond to IEOVs of  $42.9 \text{ AU}^3$  for an inert population and  $1411 \text{ AU}^3$  for an active population by solving equation 2.12 for  $\tilde{V}$  (Table 2.3).

Population	$N_S(\alpha, H')$	$\rho_{IS}^{C.L.}(\alpha, H') (AU^{-3})$	IEOV ( $AU^3$ )
Inert (0 ISOs)	28.11	$5.4 * 10^{-2}$	42.9
Active (0 ISOs)	948.75	$1.6 * 10^{-3}$	1,411
Inert (1 ISOs)	28.11	$8.4 * 10^{-2}$	42.9
Active (1 ISOs)	948.75	$2.5 * 10^{-3}$	1,4311
Inert (2 ISOs)	28.11	$1.1 * 10^{-1}$	42.9
Active (2 ISOs)	948.75	$3.3 * 10^{-3}$	1,4311

Table 2.3: Summary of Number of Expected ISOs, 90% Confidence Limit Density, and Volume for each population. For each new discovery, the number density increased while the IEOV was constant (Engelhardt 2014).

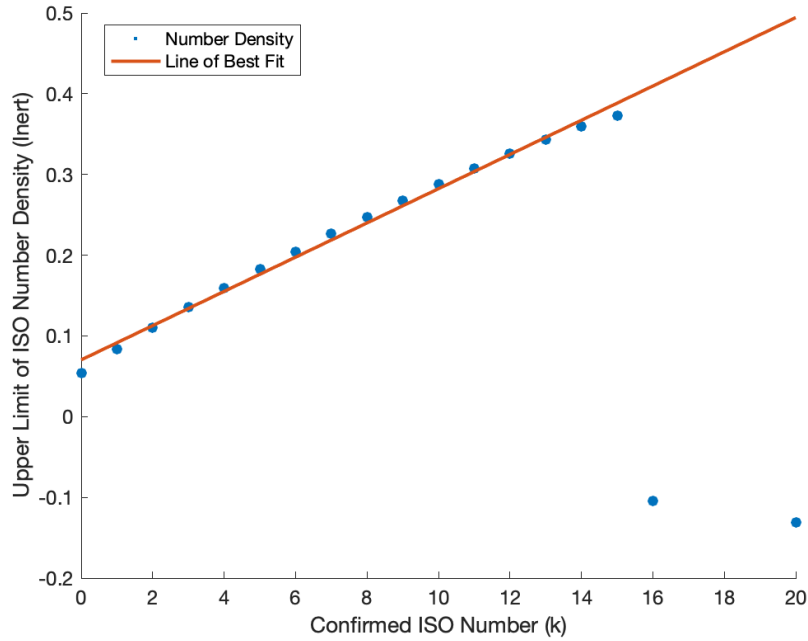
The same procedure was repeated for a different number of confirmed ISOs until the physical limit of the system was reached at  $k=16$  as described. As expected, the upper limit of the number density increased with each new confirmed event,  $k$  (Figure 2-6). For the inert population, the upper limit of the number density increased linearly with increased events with the relationship

$$\rho_{IS}^{C.L.}(\alpha, H') = 0.0212k + 0.070 \quad (2.22)$$

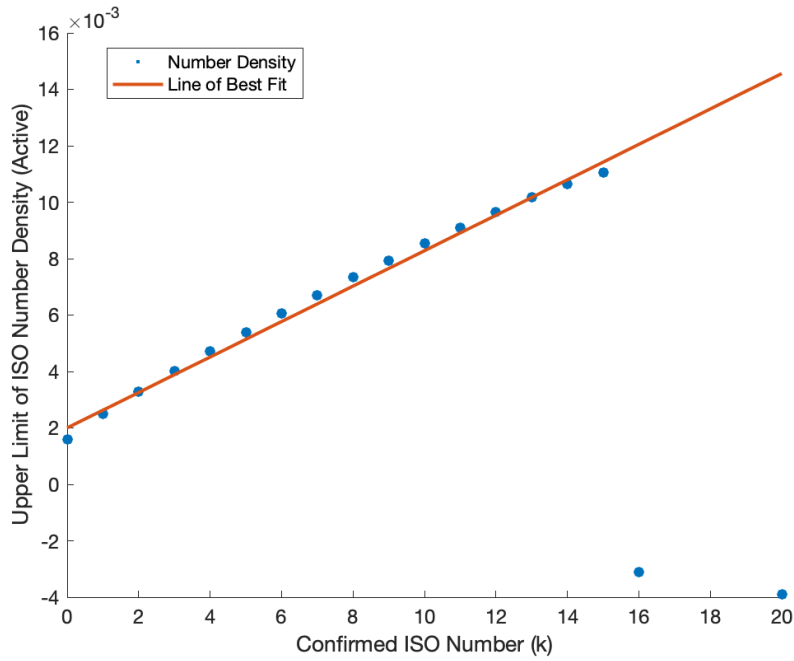
with an  $R^2$  value of 0.994. Similarly, the active population showed that the upper limit of the number density again increased linearly with increased events with the relationship

$$\rho_{IS}^{C.L.}(\alpha, H') = 6.28 * 10^{-4}k + 2.08 * 10^{-3} \quad (2.23)$$

with an  $R^2$  value of 0.994. The IEOV for each  $k$  value was calculated and found to be equivalent. Overall, each population shows the expected trend in number density and can be used for future estimations of number density as more ISOs are discovered.



(a) Inert ISO Population



(b) Active ISO Population

Figure 2-8: For both populations,  $\rho_{IS}^{C,L}(\alpha, H')$  increased with the number of known ISO events ( $k$ ). At 16 known events, the value becomes unphysical, likely due to an error in invoking a Poisson Distribution. The orange line shows the line of best fit for each number density which is shown by the blue dots. For (a), the relationship was  $\rho_{IS}^{C,L}(\alpha, H') = 0.0212k + 0.070$  and for (b),  $\rho_{IS}^{C,L}(\alpha, H') = 6.28 * 10^{-4}k + 2.08 * 10^{-3}$ .

# Chapter 3

## Discussion & Conclusion

### 3.1 Discussion

#### 3.1.1 Number Density Comparisons

After incorporating the two confirmed ISOs into the number density equation, the inert population showed an upper limit of  $0.11 \text{ AU}^{-3}$  and the active population showed an upper limit of  $3 * 10^{-3} \text{ AU}^{-3}$ . These estimates are approximately 2x the values originally calculated by Engelhardt on which this work is based. As a result, the number density estimation after accounting for 'Oumuamua and Borisov for the active population is still on the same order of magnitude for many other estimations while the inert population is an order of magnitude higher (Do 2018; Zwart 2018, McGlynn and Chapman 1989; Jewitt 2003). Given that the calculated values are larger than the maximum values originally estimated, the updated number densities are further away from the estimates of  $10^{-4} \text{ AU}^{-3}$  and  $10^{-6} \text{ AU}^{-3}$ , providing further proof that these values are too small (Hughes 2001; Stern 1990; Moro-Martín 2009).

As more ISOs are discovered, the number density continues to increase, reaching a maximum of  $0.37 \text{ AU}^{-3}$  for an inert population and  $1.1 * 10^{-2} \text{ AU}^{-3}$  for an active population. These values are larger than all other estimates by an order of magnitude, reinforcing a higher upper limit than previously estimated.

### 3.1.2 Future Estimations with New Surveys

#### Large Synoptic Space Telescope (LSST)

Set to enter full survey operations in 2023, the Large Synoptic Space Telescope (LSST) offers an opportunity for the upper limit number density of ISOs to continue to increase by providing better resolution, better tracking, and additional observation time (Myers 2011). As a result of its larger mirror, LSST's resolution will be superior to that of PS1 and it is expected to reach higher limiting magnitudes, allowing for more accurate detection of astronomical bodies including ISOs. Additionally, the MOPS system on LSST is equipped with automatic tracklet detection unlike PS1 which further increases the detection efficiency of ISOs. These improvements are coupled with an increase in observation time which is essential for making astronomical discoveries.

Currently, an exact percentage improvement in LSST over PS1 is hard to calculate using the described methods as the realistic efficiencies of various filters in LSST are not easily calculated or publicly available. The filters are similar to PS1 in that both surveys use g, r, i, z, and y filters (LSST 2021; Engelhardt 2014). However, LSST uses a u filter in place of PS1's w filter. This filter difference between the systems should not be an issue as the highest fraction of objects were detected through MOPS simulation in the [r,r] filter which both surveys share (Figure 2-2).

This efficiency value is likely to be more easily calculated in the future after the telescope has been begun surveying the sky and a more accurate understanding of how the LSST MOPS realistically performs is available. When those numbers are available, this calculation is easily redone by first recreating synthetic ISOs from a different initialization point. However, the future launch date is unknown and has been changed frequently in past. Then, the synthetic ISOs can be brought through the same process to determine a new upper limit number density.

## Other Survey Projects

In addition to LSST, future telescopes offer the chance for high resolution observations based on their large mirror sizes (Figure 3-1). Within the next decade, the Giant Magellan Telescope, the Thirty Meter Telescope, and the European Extremely Large Telescope are set to see their first light and begin observations (European Southern Observatory 2016). Similar to the relationship between PS1 and LSST, these surveys are much larger than LSST and should increase the upper limit number density as a result.

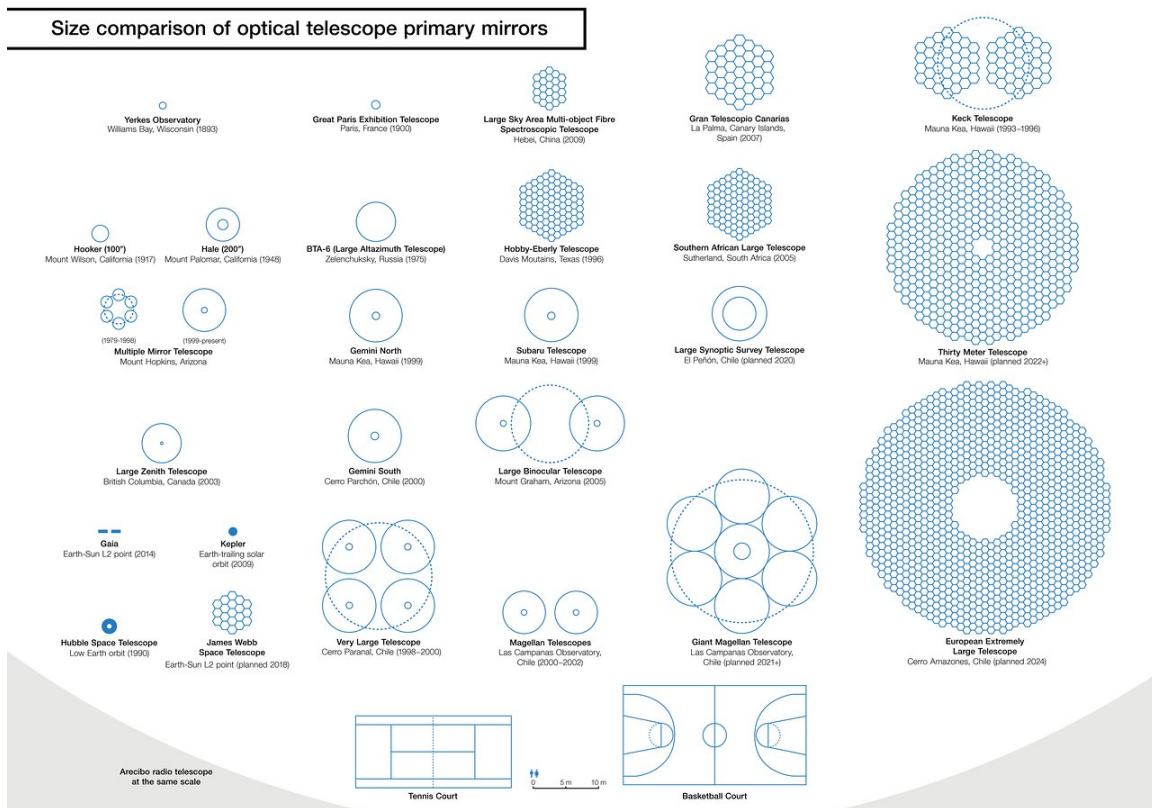


Figure 3-1: Telescopes larger than LSST are under construction now and planned to begin observation within the next decade. These are expected to have higher resolutions, increasing the chances of detecting ISOs (European Southern Observatory 2016).

## 3.2 Conclusion

In summary, an increase in sightings of ISOs and in telescope resolution has and will lead to an increase in the observational upper limit of ISO number density. Currently, the number density can be estimated as  $0.11 \text{ AU}^{-3}$  and  $3 * 10^{-3} \text{ AU}^{-3}$  for inert and active populations of ISOs, respectively. These values are in concordance with previous literature estimates including Engelhardt's "Setting an Observational Upper Limit to the Number Density of Interstellar Objects" in which this work is based upon.

Given the increase in number density and projected future increase, the number density provides a strong argument for engineering projects such as the Dynamic Orbital Slingshot concept currently underway. Projects such as these will allow for ISOs to be studied more closely, revealing important information about planetary formation and star system history from the perspective of an outside visitor.

# Bibliography

- Engelhardt, Toni. Setting an Observational Upper Limit to the Number Density of Interstellar Objects. University of Hawai'i at Mānoa. 2014.
- Engelhardt, Toni et al. An Observational Upper Limit on the Interstellar Number Density of Asteroids and Comets. *The Astronomical Journal*, 153:133. 2017.
- European Southern Observatory (ESO). Size Comparison between the E-ELT and Other Telescope Mirrors. ESO. 2016.
- Hughes, David. The magnitude distribution, perihelion distribution and flux of long-period comets. *Monthly Notices of the Royal Astronomical Society*, 326(2):, pp. 15–523, 2001.
- Jewitt, David. Project Pan-STARRS and the Outer Solar System. *Earth, Moon, and Planets*, 92(1-4), pp. 465–476, 2003.
- McGlynn, Thomas. Chapman, Robert. On the nondetection of extrasolar comets. *The Astrophysical Journal*, 346:L105–L108, 1989.
- Moro-Martín, Amaya et al. Will the Large Synoptic Survey Telescope detect extrasolar planetesimals entering the solar system? *The Astrophysical Journal*, 704(1), pp. 733, 2009.
- National Aeronautics and Space Administration (NASA). In Depth - 'Oumuamua. NASA. 2019.
- National Aeronautics and Space Administration (NASA). In Depth - Borisov. NASA. 2020.
- Linares, Richard. “Dynamic Orbital Slingshot for Rendezvous with Interstellar Objects.” NASA. 2020.
- Large Synoptic Survey Telescope (LSST). Technical Details. Rubin Observatory. 2020.
- Myers, Jonathan et al. “Moving Object Pipeline System Design.” Rubin Observatory. 2011.
- National Aeronautics and Space Administration (NASA). Newly Discovered Comet Is Likely Interstellar Visitor. NASA. 2019.
- National Aeronautics and Space Administration (NASA). Trajectories and Orbits. NASA. 1958.
- Stern, S. Alan. On the number density of interstellar comets as a constraint on the formation rate of planetary systems. *Publications of the Astronomical Society of the Pacific*, pp. 793–795, 1990.
- Zwart, S. Portegies et al. The Origin of Interstellar Asteroidal Objects like 1I/2017 U1 'Oumuamua. ArXiv PrePrint, 2018.

Zuluaga, Jorge I. et al. A General Method for Assessing the Origin of Interstellar Small Bodies: The Case of 1I/2017 U1 ('Oumuamua). *The Astronomical Journal*, 155(6), pp. 236, 2018.